Engineering Analysis with Boundary Elements 137 (2022) 29–40

Contents lists available at ScienceDirect

Engineering Analysis with Boundary Elements

journal homepage: www.elsevier.com/locate/enganabound

Analysis of stress singularity in adhesive joints using meshless methods

L.D.C. Ramalho [a,*], J.M.M. Dionísio [b], I.J. Sánchez-Arce [a], R.D.S.G. Campilho [a,b], J. Belinha [a,b]

[a] INEGI: Instituto de Engenharia Mecanica e Gestao Industrial – Pólo FEUP, Rua Dr. Roberto Frias, s/n, 400, Porto 4200-465, Portugal
[b] Departamento de Engenharia Mecânica, Instituto Superior de Engenharia do Porto, Instituto Politécnico do Porto, Rua Dr. António Bernardino de Almeida, 431, Porto 4200-072, Portugal

ARTICLE INFO

Keywords:
ISSF criterion
RPIM
Adhesive joints
Single lap joints
Meshless methods

ABSTRACT

Recent years saw a rise in the application of bonding techniques in the engineering industry. This fact is due to the various advantages of this technique when compared to traditional joining methods, such as riveting or bolting. The growth of bonding methods demands faster and more powerful tools to analyze the behavior of products. For that reason, adhesive joints have been the subject of intensive investigation over the past few years. Recently, a fracture mechanics based approach emerged with great potential to evaluate joint behavior, called Intesity of Singular Stress Fields (ISSF), similar to the Stress Intensity Factor (SIF) concept. However, it allows the study of multi-material corners and does not require an initial crack. This approach was not yet tested with meshless methods. The present work intends to fill this gap, resorting to the Radial Point Interpolation Method (RPIM). With this purpose, adhesive joints with four different overlap lengths (L_O) bonded with a brittle adhesive were studied. The interface corner's stresses were also evaluated. The predicted strengths were compared with the experimental data to assess the accuracy of the applied methods. In conclusion, the ISSF criterion proved to be applicable to meshless methods, namely the RPIM.

1. Introduction

Recent centuries brought adhesive technology to the engineering panorama. However, this technique goes back to the time of the Neandertals, where they used resin collected from pine trees to glue their tools. Nowadays, it is applied to a wide range of industries, and it is hard to imagine a product that does not incorporate adhesive bonding [1]. The spread of adhesive bonding technology is mainly due to the aeronautical industry that introduced the concept of structural bonding. This notion highlighted several advantages of this joining process. The primary profit is in terms of the bonding weight. For the aeronautical industry, this characteristic is vital. Another distinctive quality is the more uniform stress distribution along the bonded area's width, allowing higher stiffness and improved load transmission [2]. Also, the non-necessity of drilling or damaging the adherends (including composites) for the joining process is highly convenient. Even so, like any other technology, this procedure has some associated issues. The most significant ones are the typical disassembly impossibility and the required curing time [3]. Nonetheless, the benefits of this technology are far more important than its weaknesses. For that reason, this technique is nowadays widely spread throughout a wide range of engineering fields, namely aeronautical, automotive, aerospace, civil and electronics [4].

When this technology emerged, computational resources were limited. Thus, the first analyses were performed through analytical models. Volkersen [5] was a pioneer in this area and developed the first model to analyze the stress distributions along the adhesive layer. He introduced the concept of differential shear [6], in which the adherends are considered elastic instead of rigid. Other researchers improved Volkersen's work, namely Goland and Reissner [7] and Hart-Smith [8]. However, these models had complex formulations or were very simple, but many simplifications were considered. De Sousa et al. [9] studied different analytical models and performed a comparison between them. The results showed that the Hart-Smith plastic model accurately predicts the strength increase with the overlap length (L_O) when dealing with brittle adhesives. When analysing ductile adhesives, the global yielding failure criterion [10] was the only one to accurately predict the joint strength for different L_O. The limitations of the analytical models meant that problems with a higher degree of complexity were impossible to solve. These limitations paved the way for the appearance of numerical methods. The most widespread numerical technique is the Finite Element Method (FEM) [11]. With this method, there are different

* Corresponding author.
E-mail address: lramalho@inegi.up.pt (L.D.C. Ramalho).

https://doi.org/10.1016/j.enganabound.2022.01.012
Received 6 July 2021; Received in revised form 14 December 2021; Accepted 13 January 2022
Available online 21 January 2022

approaches to evaluate the failure of adhesive joints, like continuum mechanics [12], damage mechanics [13], or the eXtended Finite Element Method (XFEM) [14]. Nonetheless, the most frequent method employed is Cohesive Zone modeling (CZM) [15]. This approach is usually characterized by paired nodes that behave accordingly to a cohesive law. The CZM approach includes continuum mechanics principles for damage initiation and fracture mechanics principles for crack propagation, establishing a softening relationship between stresses and strains, thus simulating gradual degradation of the material's mechanical properties. The cohesive law can assume different shapes, such as triangular, linear-parabolic, polynomial, exponential and trapezoidal [16]. The most basic shape is the triangular shape and it produces excellent results when treating brittle adhesives. Zhang et al. [17] examined different law shapes in Double-Cantilever Beam (DCB) and butt-joints, bonded with brittle and ductile adhesives. The results showed a significant influence of the law shape in the butt joint strength predictions, while for DCB the influence was smaller but still important. As expected, the triangular shape presented the best results for the brittle adhesives. For the ductile adhesives, the exponential law showed more suitability for the butt joints and the trapezoidal law for the DCB joints.

Another relevant approach to adhesive joint failure is fracture mechanics. Usually, two concepts are used in fracture mechanics: the Stress Intensity Factor (SIF) and the Strain Energy Release Rate (SERR). These techniques allow the evaluation of discontinuities in materials, such as re-entrant corners at the adhesive-adherend interface or defects. The determination of the SIF or the SERR can be performed through routines like the J-integral [18] or the Virtual Crack Closure Technique (VCCT) [19]. More recently, a new fracture mechanics based model arose that combines stress and energy criteria, called Finite Fracture Mechanics (FFM) [20]. In this model, an energetic and a stress criterion must be concurrently fulfilled for crack initiation.

The fracture mechanics approaches include the Intensity of Singular Stress Fields (ISSF) or General Stress Intensity Factor (GSIF). This approach can determine the singularity exponent in sharp material interface corners present in many adhesive joints and its intensity. Williams [21] and Bogy [22] published the first works dealing with this singularity. Many authors use the ISSF to only study the stresses and displacements around the interface corners of adhesive joints. Such is the case of Noda et al. [23], which studied the ISSF in single-lap joints (SLJ) and butt joints. In SLJ, they experimented with different L_O and adhesive thicknesses (t_A). It was shown that assuming an equal loading force, the ISSF remains almost constant for different t_A, but L_O affected the ISSF. Actually, for L_O<15 mm, the ISSF increased with increasing L_O, while for $L_O \geq 15$ mm, the ISSF decreased with increasing L_O. Goglio and Rossetto [24] proposed a purely numerical method to determine the singularity exponent (λ) and its intensity (H). This approach has the advantage that only a simple numerical simulation is needed, but it is not as precise. Moreover, depending on the stress component and angle used to perform this estimation, differences in the theoretical values of λ can be found. Thus, the choice of these parameters has to be careful. In addition to studying the stresses and displacements around an adhesive joint's corner, the ISSF has also been used to predict the strength of adhesive joints. Askarinejad et al. [25] used the ISSF to predict the strength of Thick Adherend Shear Tests (TAST) specimens without an initial crack and also used the conventional SIF for TAST specimens with initial cracks with different lengths. In both cases, the strength predictions were in line with the experimental strength. Akhavan-Safar et al. [26] proposed that the critical ISSF (H_c) could be determined by performing numerical simulations with the experimental failure loads imposed. In that work, they tested SLJ with varying geometrical parameters, including L_O, t_A, substrate thickness and free length. The authors proposed that H_c depends on those geometrical parameters and recommended a function that could take these parameters into account to determine the maximum load (P_m). This function predicted the strength of the joints with good accuracy.

All the approaches mentioned before are generally applied through the FEM. However, a new class of discrete numerical techniques has been gaining prominence: meshless methods. The necessity of discretising the studied object into elements constrains the use of FEM. For example, an object with large deformations generates accuracy loss in the obtained results due to distortions in the elements [27]. Thence, the rise of meshless methods that do not rely on a structured mesh. One of the most studied meshless approaches is the Radial Point Interpolation Method (RPIM) [28]. The Natural Neighbor Radial Point Interpolation Method (NNRPIM) is a recent approach that combines the RPIM with the concept of natural neighbors [29]. This method considers the concept of "influence-cells" instead of "influence-domain" to impose nodal connectivity [30]. For the definition of the influence-cells, Voronoï diagrams and Delaunay tessellation are used. These methods have been applied to the study of adhesive joints in recent years. In 2017, Farahani et al. [31] used FEM and RPIM to determine the SIF for a compact tension specimen (CT) after determining these parameters experimentally with a fatigue crack growth test with Thermoelastic Stress Analysis (TSA). The two numerical methods presented similar results that agreed very well with the experimental data. Ramalho et al. [32] also applied this approach to composite adhesive SLJ with a brittle adhesive and different L_O. They overcame the difficulty of applying RPIM to bi-material problems by restricting the influence domains in the interface region between materials. With this procedure, the stresses obtained with the RPIM were very similar to the ones of FEM. Sánchez-Arce et al. [33] resorted to the NNRPIM to analyze adhesive joints. They measured experimental data of SLJ corresponding to four different L_O with a brittle adhesive. Then, they simulated the geometries resorting to the FEM and NNRPIM. By comparing the results, it was concluded that the results were very similar between the two methods, with a maximum difference observed in the strength of 2%, proving that the NNRPIM is suitable for this analysis. The maximum peak shear stress difference between FEM and NNRPIM predictions was 6.6%, indicating the method's suitability. The Boundary Element Method (BEM) is another discrete technique alternative to the FEM. Very recently, Wen et al. [34] resorted to BEM to analyze curved cracks. Until today, BEM has been applied to investigate the most diverse areas, such as composite materials [35–37].

The present work aims to evaluate the applicability of the ISSF criterion to meshless methods. In that regard, SLJ with different L_O bonded with a brittle adhesive were studied. The influence of L_O in the experimental results was analyzed. To predict the joint strength, the ISSF criterion was used. This method was numerically applied through the RPIM. The different steps necessary for these applications are also covered. In order to evaluate the influence of the discretization in the final results, two meshes with different levels of refinement were assessed. A comparison between the analytically obtained stresses and the ones determined numerically using RPIM was performed. Finally, the predicted strengths were compared with the experimental data to validate the applicability of the ISSF criterion to meshless methods, namely the RPIM. The literature survey made during the elaboration of this work showed that the use of the ISSF as a criterion to determine joint strength was only previously attempted in two works, dedicted to predict the strength of TAST specimens [25] and SLJ [26]. Furthermore, those two works calculated the ISSF from FEM simulations. To the authors' best knowledge, the present work is the first work where the ISSF is calculated from a RPIM simulation. Additionally, the effect of L_O on the critical ISSF of SLJ was only previously studied in [26], which is

insufficient to establish a definitive conclusion. This work uses a different adhesive/adherend combination, so the data gathered regarding the effect of L_O should clarify if the increase of the critical ISSF with LO found in Ref. [26] is universal, or if it was particular to the material combination used in that work.

2. Experimental setup

2.1. SLJ geometry and dimensions

The meshless ISSF technique for strength prediction was validated with experiments, considering aluminium adherend SLJs bonded with a strong and brittle adhesive (Araldite® AV138). Fig. 1 overviews the base geometry, dimensions (L_O was varied between 12.5 and 50 mm) and boundary conditions (BC). The applied BC aimed to emulate experimental testing under displacement control, and thus they involved clamping the left joint end, while a displacement (δ) was applied to the right end. Contrarily to L_O, the other base dimensions were kept constant: adherends' thickness t_P=3 mm, adhesive thickness t_A=0.2 mm, total joint length L_T=180 mm and joint width $B = 25$ mm (B is not shown in the figure).

2.2. Adherend and adhesive materials

The AW6082-T651 aluminium alloy was selected as the base material for the adherends. This aluminium alloy has medium strength and ductility and is used in structural applications in the naval, automotive, and railroad industries. The unidirectional tensile behavior of this material was acquired from former works [38,39] by dogbone bulk tests leading to the characterization up to failure by means of the stress-strain (σ-ε) curves. Data analysis led to the properties defined in Table 1, including Young's modulus (E), the Poisson coefficient (ν), the tensile yield stress (σ_y), the tensile strength (σ_f) and the tensile failure strain (ε_f).

The SLJs were bonded with a strong yet brittle epoxy adhesive: the Araldite® AV138 from Huntsman®. Actually, the AV138 has $\sigma_f \approx 40$ MPa, which can be considered a high standard for epoxy adhesives, although it is brittle. As a result, the performance can be poor when applied to bonded joints, typically experiencing large peak stresses due to the sharp corners and compliance difference between adjacent materials. Previous studies [38] showed that adhesives that fail to enter the plastic regime give usually worse results than less strong but ductile adhesives, particularly for large L_O, due to the associated peak stresses arising at the overlap edges. This statement is also valid for small L_O, but to a smaller extent, since the stress distributions in the adhesive layer flatten, thus decreasing the relevance of ductility. Thus, brittle adhesives can compete with ductile ones for small L_O. The Araldite® AV138 was properly characterized in a former work by De Sousa et al. [9] to obtain the necessary input properties for strength prediction. The mechanical tests included bulk tensile and TAST testing. The bulk tests were executed following the NF T 76-142 French standard, which gives the specimens' geometry and recommended manufacturing method, leading to estimations of E, σ_y, σ_f and ε_f. On the other hand, the TAST tests led to the shear elastic modulus (G), shear yield stress (τ_y), shear strength (τ_f) and shear failure strain (γ_f). These tests followed the 11,003–2:1999 ISO standard (for manufacturing and test protocols). The TAST specimens were thus assembled, aligned and cured in a jig with side pins to assure the longitudinal alignment. The adherend material for these specimens was steel (DIN C45E), whose stiffness manages to almost eliminate adherend strains that affect the stiffness calculations. All the obtained properties of this adhesive are presented in Table 2.

Table 1
Tensile properties of the AW6082-T651 aluminium alloy [38,39].

Property	Value
E (GPa)	70.1 ± 0.83
ν	0.30
σ_y (MPa)	261.67 ± 7.65
σ_f (MPa)	324.00 ± 0.16
ε_f (%)	21.70 ± 4.24

2.3. Joint production and testing

Joint manufacturing and testing is a highly relevant step of numerical validation works to be able to produce reliable and repeatable results for comparison with the output of the numerical simulations for a clear assessment. Thus, these procedures should be carefully planned and executed, following the current standards and practices. The initial step consisted of cutting the adherends with dimensions of 140×25 mm^2. Before bonding, the adherends were sandblasted with corundum sand particles to remove the oxide layer and dirt/contaminants, which could prevent a good bond and trigger premature adhesive (interfacial) failures. Following, before bonding the adherends in a steel jig, preparation was required. Actually, for the fabricated joints to achieve t_A=0.2

Table 2
Properties of the Araldite® AV138 [9].

Property	AV138
E (GPa)	4.89 ± 0.81
ν	0.35[1]
σ_y (MPa)	36.49 ± 2.47
σ_f (MPa)	39.45 ± 3.18
ε_f (%)	1.21 ± 0.10
G (GPa)	1.56 ± 0.01
τ_y (MPa)	25.1 ± 0.33
τ_f (MPa)	30.2 ± 0.40
γ_f (%)	7.8 ± 0.7

[1] Data from the manufacturer.

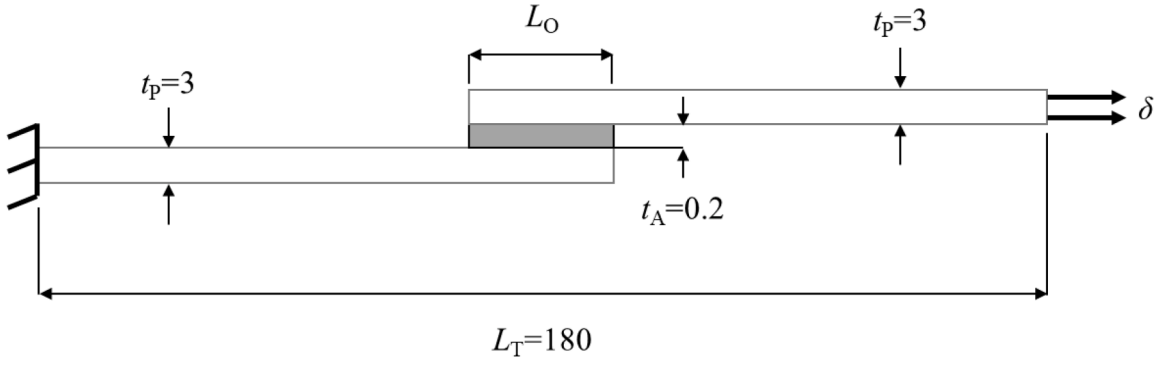

Fig. 1. SLJ geometry and dimensions in mm (L_O was varied between 12.5 and 50 mm).

mm, it was necessary to place Teflon® wire, having a diameter of 0.2 mm, between adherends during the curing process. These stoppers were placed between 1 and 2 mm inside the overlap region to provide the minimum disruption to stress distributions in the adhesive layer but keeping the surfaces separated apart by 0.2 mm when applying pressure to the joints. To help with this process, the adherends were inserted in the jig with lateral guidance to prevent misalignments. After applying the adhesive to the lower adherend in the jig, the top adherend was slowly set in position and manually pressured against each other, such that the excess adhesive could flow out of the bonding length without the creation of voids. The specimens were then pressured at the overlap with grips and left to cure at room temperature. After curing, the excess adhesive was removed by milling to achieve the geometry of Fig. 1 as closely as possible. The joints were tested in a Universal Testing Machine (UTM), considering L_T=180 mm for all joint configurations. A Shimadzu AG-X 100 UTM, equipped with a 100 kN load cell, was used. Loading was performed under displacement control, with a constant velocity of 1 mm/min. Each joint configuration gave at least 4 valid tests, which enabled calculating the average failure load and considering it the experimental P_m for numerical model validation.

3. Numerical analysis

3.1. RPIM formulation

The implementation of the RPIM is similar to the FEM, representing an advantage to adapt existing FEM software to RPIM. It all starts with the discretization of a domain Ω into a nodal set $\mathbf{N} = \{n_1, n_2, \ldots, n_N\}$ with coordinates $\mathbf{X} = \{x_1, x_2, \ldots, x_N\} \in \Omega$. Afterwards, it is necessary to define a background integration grid used to create the integration points. For instance, one can use the finite element mesh as the RPIM integration grid. The integration technique used to perform the numerical integration of the stiffness matrix was the Gauss-Legendre quadrature. Within this technique, the grid-cells created are filled with integration points, following the Gauss-Legendre quadrature rule. Thus, inside each integration cell, 2 × 2 integration points were inserted as Fig. 2(a) shows. The procedure applied within this rule can be found in detail in the literature [30,40]. Then, the influence domain of each integration point is determined. The FEM counterpart of influence domains is how the elements are organized in a matrix. The influence domain of an integration point consists of a set of nodes used to construct the RPIM shape functions. There are several different techniques to determine the influence domains, but each influence domain should possess a similar number of nodes. Due to that, in the simulations performed in this work, the influence domains of each integration point are composed of the 16 nodes closest to it, which is within the advised number of nodes per influence domain found in the literature [30,41]. It is important to note that any given node possibly belongs to several influence domains. This concept (called domain overlapping) allows imposing the nodal connectivity [30]. The concepts described previously are presented in Fig. 2 for two example integration points.

In addition to the influence domains vs elements, the RPIM and the FEM also differ in how the shape functions are determined, which is described in detail in Section 3.1.1. Apart from that, the implementation of the RPIM is very similar to the FEM implementation. A global stiffness matrix is assembled from all the local stiffness matrices obtained using the shape functions and material properties. The natural (imposed forces) and essential (displacement constraints/imposition) boundary conditions are imposed, and the global system of equations is solved. These steps are performed in the same manner as in the FEM.

3.1.1. Shape functions

For an integration point $x_I \subset \mathbb{R}^d$, in the domain Ω, presented in Section 3.1, any field variable $u(\boldsymbol{x})$ can be interpolated using the radial point interpolation technique[30]. Thus, interpolated value of an integration point $\boldsymbol{x}_I$, $u(\boldsymbol{x}_I)$, can be obtained with:

$$u(\boldsymbol{x}_I) = \boldsymbol{r}(\boldsymbol{x}_I)^T \boldsymbol{a}(\boldsymbol{x}_I) + \boldsymbol{p}(\boldsymbol{x}_I)^T \boldsymbol{b}(\boldsymbol{x}_I), \quad (1)$$

Being $\boldsymbol{r}(\boldsymbol{x}_I)$ the radial basis function vector, $\boldsymbol{p}(\boldsymbol{x}_I)$ the polynomial basis function vector and $\boldsymbol{a}(\boldsymbol{x}_I)$ and $\boldsymbol{b}(\boldsymbol{x}_I)$ the non-constant coefficients of $\boldsymbol{r}(\boldsymbol{x}_I)$ and $\boldsymbol{p}(\boldsymbol{x}_I)$, respectively. While $\boldsymbol{a}(\boldsymbol{x}_I)$ and $\boldsymbol{r}(\boldsymbol{x}_I)$ will have a size equal to $[n \times 1]$, $\boldsymbol{b}(\boldsymbol{x}_I)$ and $\boldsymbol{p}(\boldsymbol{x}_I)$ will have a size equal to $[m \times 1]$. The total

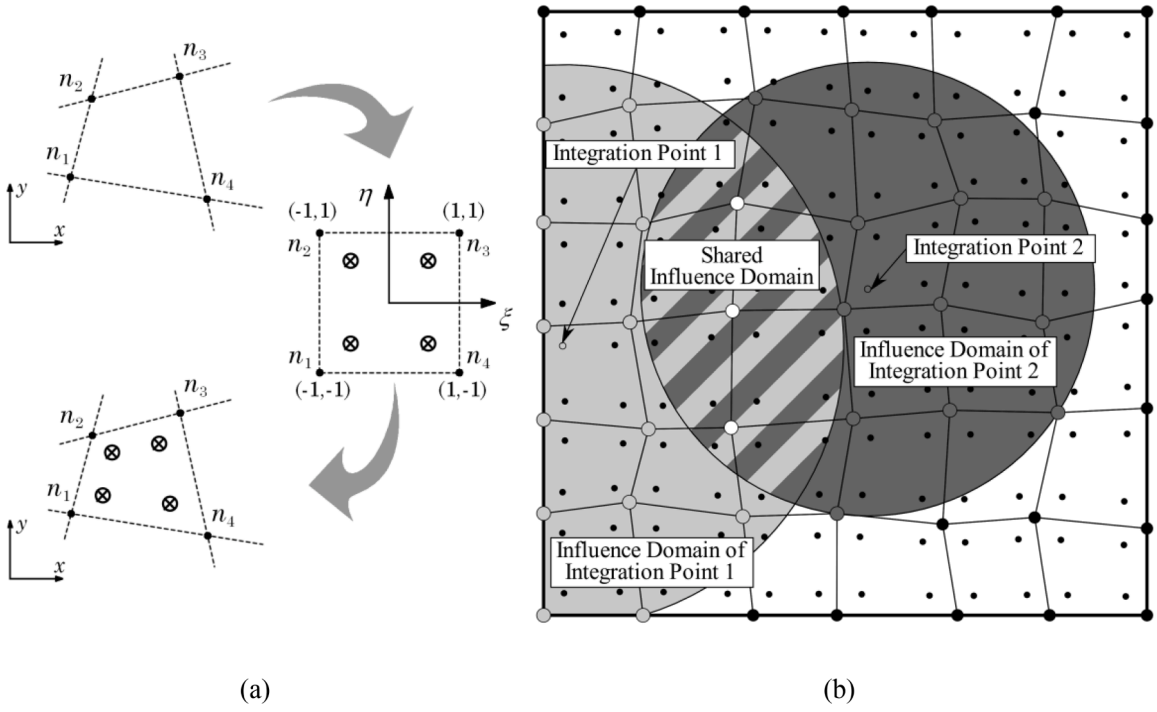

Fig. 2. (a) RPIM 2 × 2 integration scheme. (b)Representation of RPIM concepts.

number of nodes in the influence domain of $\boldsymbol{x}_I$ is denoted by n, while the number of monomials of the complete polynomial basis, defined according to Pascal's triangle, by m.

In this work, a linear polynomial basis was used in the RPI formulation ($p(\boldsymbol{x}) = \{1xy\}^T, m = 3$), since a higher polynomial basis results in longer computational times and the results did not change significantly with them. The Radial Basis Function (RBF) used in this work was the multi-quadrics (MQ) RBF, but there are other alternatives such as the Gaussian RBF or the thin plate spline RBF [30]. The MQ-RBF is defined as $r_i(x_I) = (d_{iI}^2 + (\gamma d_a)^2)^p$ [30], being γ and p the MQ-RBF shape parameters, d_a the integration weight of the interest point $\boldsymbol{x}_I$ and d_{iI} the Euclidean norm between node i and the integration point I. For the RPIM, the parameters that provide the best results are γ=1.03 and p = 1.42, as suggested by Wang and Liu [42]. Thus, these values are used in this work. Applying Eq. (1) to each node of inside the influence domain of $\boldsymbol{x}_I$, leads to the following system of equations [30]:

$$\boldsymbol{Ra}(\boldsymbol{x}_I) + \boldsymbol{Pb}(\boldsymbol{x}_I) = \boldsymbol{u}_s, \tag{2}$$

where $\boldsymbol{u}_s^T = \{\, u_1 \quad u_2 \quad \dots \quad u_n \,\}$ is a vector with the field function values at each node inside the influence domain of $\boldsymbol{x}_I$, which can be the displacement, velocity, temperature or another variable, depending on the problem under analysis. The MQ-RBF moment matrix, $\boldsymbol{R}$, will have a size equal to $n \times n$, while the polynomial moment matrix, $\boldsymbol{P}$, will have a size equal to $m \times n$. To obtain a unique solution it is necessary to add another set of equations [30]:

$$\boldsymbol{P}^T \boldsymbol{a}(\boldsymbol{x}_I) = z, \tag{3}$$

being $\boldsymbol{z}$ a null vector with size $[m \times 1]$. The combination of Eqs. (2) and (3) leads to the final set of equations [30]:

$$\begin{bmatrix} \boldsymbol{R} & \boldsymbol{P} \\ \boldsymbol{P}^T & \boldsymbol{Z} \end{bmatrix} \begin{Bmatrix} \boldsymbol{a}(\boldsymbol{x}_I) \\ \boldsymbol{b}(\boldsymbol{x}_I) \end{Bmatrix} = \boldsymbol{M}_T \begin{Bmatrix} \boldsymbol{a}(\boldsymbol{x}_I) \\ \boldsymbol{b}(\boldsymbol{x}_I) \end{Bmatrix} = \begin{Bmatrix} \boldsymbol{u}_s \\ z \end{Bmatrix}, \tag{4}$$

being $\boldsymbol{Z}$ a null matrix with size $[m \times m]$. [30]. Then, $\boldsymbol{a}(\boldsymbol{x}_I)$ and $\boldsymbol{b}(\boldsymbol{x}_I)$ can be obtained:

$$\begin{Bmatrix} \boldsymbol{a}(\boldsymbol{x}_I) \\ \boldsymbol{b}(\boldsymbol{x}_I) \end{Bmatrix} = \boldsymbol{M}_T^{-1} \begin{Bmatrix} \boldsymbol{u}_s \\ z \end{Bmatrix}. \tag{5}$$

By substituting $\boldsymbol{M}_T^{-1} \{\, \boldsymbol{u}_s \quad z \,\}^T$ into Eq. (1), the following is obtained:

$$u(\boldsymbol{x}_I) = \{\, \boldsymbol{r}(\boldsymbol{x}_I)^T \quad \boldsymbol{p}(\boldsymbol{x}_I)^T \,\} \, \boldsymbol{M}_T^{-1} \begin{Bmatrix} \boldsymbol{u}_s \\ z \end{Bmatrix}. \tag{6}$$

The field function value for an interest point $\boldsymbol{x}_I$ is interpolated using the shape function values at the nodes inside the influence domain of $\boldsymbol{x}_I$, which can be identified in Eq. (6) [30]:

$$u(\boldsymbol{x}_I) = \{\, \boldsymbol{\Phi}(\boldsymbol{x}_I)^T \quad \boldsymbol{\Psi}(\boldsymbol{x}_I)^T \,\} \, \boldsymbol{M}_T^{-1} \begin{Bmatrix} \boldsymbol{u}_s \\ z \end{Bmatrix}, \tag{7}$$

being $\boldsymbol{\Psi}(\boldsymbol{x}_I) = \{\, \psi_1(\boldsymbol{x}_I) \quad \psi_2(\boldsymbol{x}_I) \quad \dots \quad \psi_n(\boldsymbol{x}_I) \,\}^T$ and $\boldsymbol{\Phi}(\boldsymbol{x}_I) = \{\, \varphi_1(\boldsymbol{x}_I) \quad \varphi_2(\boldsymbol{x}_I) \quad \dots \quad \varphi_n(\boldsymbol{x}_I) \,\}^T$ a by-product vector with no relevant meaning and the interpolation shape function, respectively. A more complete formulation of the RPIM, including the derivatives of the shape functions needed to solve the $\boldsymbol{Ku} = \boldsymbol{f}$ system of equations, can be found in the literature [30].

3.2. ISSF approach

The ISSF, a fracture mechanics based approach, intends to study discontinuities in materials, as explained in Section 1. The present work uses the ISSF to analyze bi-material interface corners in SLJ, such as those in Fig. 3.

The basis of the ISSF is the description of the stress, in polar coordinates (shown in Fig. 4), around an interface singularity based on the following equation:

$$\sigma_{ij} = \sum_{n=1}^{\infty} H_n r^{\lambda_n - 1} f_{ij}(\lambda_n, \theta). \tag{8}$$

It can also be used to describe the displacement, also in polar coordinates, in the same region:

$$u_j = \sum_{n=1}^{\infty} H_n r^{\lambda_n} g_j(\lambda_n, \theta), \tag{9}$$

being n the number of singularity exponents (λ), which depends on the interface corner's geometry and materials. H_n is the ISSF, or GSIF, which is a scalar value. The first step to solve this equation is the determination of λ, which are obtained by solving the following equation [43]:

$$0 = e^2 + b^2 - (\lambda c)^2 - (\lambda d)^2. \tag{10}$$

Equations e, b, c and d can be found in Appendix 1. The angles θ_1 and θ_2 in those equations are the angles of the materials in the interface corner, and α and β are the Dundurs parameters [44], which are material dependent and relate the properties of the interface corner materials, having the following definition:

$$\alpha = \frac{G_1(\kappa_2 + 1) - G_2(\kappa_1 + 1)}{G_1(\kappa_2 + 1) + G_2(\kappa_1 + 1)} \tag{11}$$

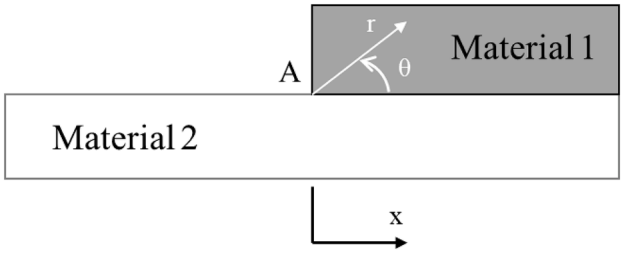

Fig. 4. Polar coordinates in a bi-material interface corner.

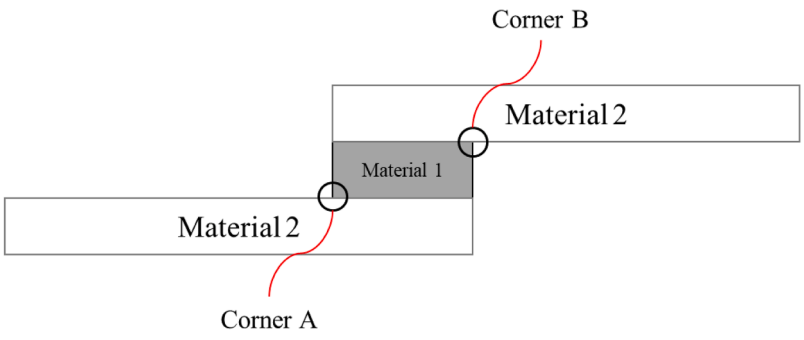

Fig. 3. Discontinuities in SLJ.

$$\beta = \frac{G_1(\kappa_2 - 1) - G_2(\kappa_1 - 1)}{G_1(\kappa_2 + 1) + G_2(\kappa_1 + 1)}, \tag{12}$$

being κ_m=3,4ν_m in plane strain cases and G_m the shear modulus of material m. The subscripts 1 and 2 in this equation represent the two different materials of the interface corner. With λ determined, the next step is the calculation of the displacement and stress functions, $f_{ij}(\lambda_n, \theta)$ and $g_j(\lambda_n, \theta)$ respectively, by solving the following system of equations:

$$\{\, g^m_{rr} \quad g^m_{\theta} \quad f^m_{rr} \quad f^m_{\theta\theta} \quad f^m_{\theta} \,\}^T = \boldsymbol{N_m X_m Y}. \tag{13}$$

Here, m indicates the material and the matrices $\boldsymbol{N}_m$ and $\boldsymbol{X}_m$, and vector $\boldsymbol{Y}$ are defined as [43]:

$$\boldsymbol{N}_m = \begin{bmatrix} \frac{(\kappa_m - \lambda)\cos([\lambda-1]\theta)}{2G_m} & \frac{(-\kappa_m + \lambda)\sin([\lambda-1]\theta)}{2G_m} & -\frac{\cos([\lambda+1]\theta)}{2G_m} & \frac{\sin([\lambda+1]\theta)}{2G_m} \\ \frac{(\kappa_m + \lambda)\sin([\lambda-1]\theta)}{2G_m} & \frac{(\kappa_m + \lambda)\cos([\lambda-1]\theta)}{2G_m} & \frac{\sin([\lambda+1]\theta)}{2G_m} & \frac{\cos([\lambda+1]\theta)}{2G_m} \\ -(\lambda^2 - 3\lambda)\cos([\lambda-1]\theta) & (\lambda^2 - 3\lambda)\sin([\lambda-1]\theta) & -\lambda\cos([\lambda+1]\theta) & \lambda\sin([\lambda+1]\theta) \\ (\lambda^2 + \lambda)\cos([\lambda-1]\theta) & -(\lambda^2 + \lambda)\sin([\lambda-1]\theta) & \lambda\cos([\lambda+1]\theta) & -\lambda\sin([\lambda+1]\theta) \\ (\lambda^2 - \lambda)\sin([\lambda-1]\theta) & (\lambda^2 - \lambda)\cos([\lambda-1]\theta) & \lambda\sin([\lambda+1]\theta) & \lambda\cos([\lambda+1]\theta) \end{bmatrix} \tag{14}$$

$$\boldsymbol{X}_1 = \begin{bmatrix} 1 & 0 \\ 0 & 1 \\ \chi_{31} & \chi_{32} \\ \chi_{41} & \chi_{42} \end{bmatrix}; \quad \boldsymbol{X}_2 = \begin{bmatrix} \chi_{51} & \chi_{52} \\ \chi_{61} & \chi_{62} \\ \chi_{71} & \chi_{72} \\ \chi_{81} & \chi_{82} \end{bmatrix}; \quad \boldsymbol{Y} = \begin{Bmatrix} y_1 \\ y_2 \end{Bmatrix}. \tag{15}$$

The components of $\boldsymbol{X}_m$ and $\boldsymbol{Y}$ are given by the equations in Appendix 2 [43].

After the two previous steps are completed, it is possible to determine H_n with the aid of a numerical simulation. In this work, this simulation was performed using the RPIM, and H_n was determined by performing an extrapolation to the corner, i.e. $r = 0$ mm, from values near it. However, there are other alternatives, such as performing a line or area integration encircling the interface corner, as in the work of Qian and Akisanya [43]. The extrapolation method requires a n number of points at different angles (θ) and at a fixed radius, equal to the number of λ, to determine H_1 to H_n using the following system of equations:

$$\begin{bmatrix} r^{\lambda_1 - 1} f_{\theta\theta}(\lambda_1, \theta_{n+1}) & \cdots & r^{\lambda_n - 1} f_{\theta\theta}(\lambda_n, \theta_{n+1}) \\ \vdots & \ddots & \vdots \\ r^{\lambda_1 - 1} f_{\theta\theta}(\lambda_1, \theta_{n+n}) & \cdots & r^{\lambda_n - 1} f_{\theta\theta}(\lambda_n, \theta_{n+n}) \end{bmatrix} \begin{Bmatrix} H_1 \\ \vdots \\ H_n \end{Bmatrix} = \begin{Bmatrix} \sigma_{\theta\theta}(r, \theta_{n+1}) \\ \vdots \\ \sigma_{\theta\theta}(r, \theta_{n+n}) \end{Bmatrix}. \tag{16}$$

With Eq. (16), $\boldsymbol{H}$ is determined for several different r, and then it is extrapolated to $r = 0$ mm from an interval where the r vs $\boldsymbol{H}$ relationship is approximately linear to obtain the true $\boldsymbol{H}$ at the interface corner.

3.3. Numerical setup

As already stated, this work aims to validate the ISSF criterion through a meshless method, in this case, the RPIM. For this purpose, a developed meshless program running in MATLAB was used. At this stage, all the necessary modeling conditions to perform the numerical analysis were defined and input into the program. The first step was the creation of the geometries. Initially, a background integration grid (equivalent to a FEM mesh) was used to create the integration points, as previously described in Section 3.1. The grid was constructed through quadrilateral elements characterized by the four points' coordinates corresponding to the vertices and the number of divisions along each dimension. These coordinates have to be precise to prevent the adherends and adhesive layer to overlap. Four geometries were created to evaluate the different L_O. Afterwards, the material properties were specified. These were described in Section 2.2 for both the aluminium and the Araldite® AV138. For this analysis, the materials were considered linear elastic. Then, the essential BC were detailed. In this manner, the left side of the SLJ was considered fixed (U_x=U_y=U_z=0), as shown in Fig. 1. On the contrary, at the right side, a prescribed displacement was imposed (U_x=δ; U_y=U_z=0).

The set of nodes that describe the geometries was assigned to finish the pre-processing for the numerical analysis. Unlike in the FEM, it was not necessary to define the type of elements that describe the geometry at this stage because, for RPIM, only the nodes are necessary. The selected nodal distribution applied intended to find a balance between resolution and computational cost. As mentioned in Section 3.1, the size of each influence domain implemented was 16 nodes. Two different refinement levels were applied to evaluate the discretization's influence in the ISSF criterion, as shown in Fig. 5(a) and (b).

The baseline discretization has approximately half the number of nodes of the refined discretization at the interface corners (Fig. 5(c)). Material interfaces can be problematic in meshless methods like the RPIM. The influence domains of an integration point on a material can significantly penetrate the other material, influencing the numerical results. Several authors have proposed solutions to this problem [45–47]. They consist of limiting the interaction between different materials' influence domains to the interfaces node layer, which was also adopted in this work. In summary, when the influence domain of a given integration point near the material interface is determined the algorithm considers the interface as a separation zone. So, if the integration point is in the adherend it will only look for nodes in the adherend or the interface, while if the integration point is in the adhesive it will only look for nodes in the adhesive or the interface. This insures that there is still connectivity between the materials, since the nodes in the interface will belong to influence domains of both materials, and that there is no influence domain penetration. An example of the influence domains near the interface with this restriction is shown in Fig. 6. All the simulations were performed under the following conditions: two-dimensional plane strain conditions, small deformations and linear elastic material behavior. After these simulations were concluded, the ISSF criterion was tested through a script implemented in MATLAB that contained the previously presented formulation in Section 3.2.

4. Results

4.1. Experimental results

After concluding the experimental tests, it was possible to analyze

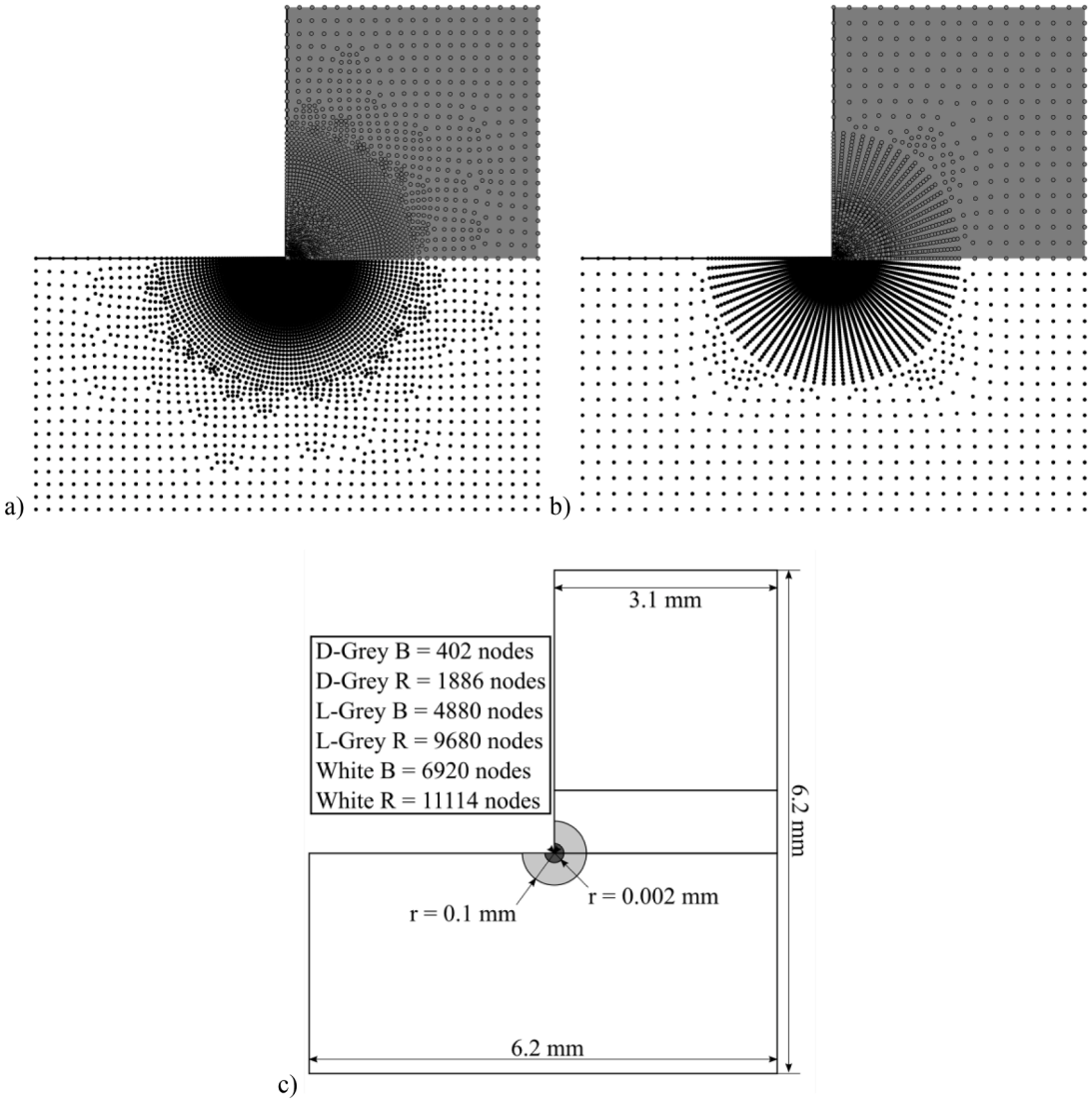

Fig. 5. Baseline (a) and refined discretizations (b) at the overlap end and mesh detail around the interface corner (c).

the type of fracture developed in the joints. A close inspection revealed that all the joints presented failure along the adhesive layer, with a visible and continuous adhesive layer on both failed adherends. These are signs of cohesive failure, indicating that joint preparation was accomplished correctly. Also, none of the joints presented plastic deformation in the adherends. The maximum sustained load (P_m) values were extracted from the load-displacement curves of every joint tested. Then, for each L_O, the average P_m was obtained along with the corresponding standard deviation, leading to the P_m vs L_O plot shown in Fig. 7. This curve presents an almost linear behavior, accompanied by a steady increase of P_m with L_O, although with a reduction of the increasing slope of P_m for higher L_O. Additionally, the P_m-L_O curve is largely non-proportional with respect to the plot origin. The reason for this phenomenon is the adhesive's brittleness or lack of ductility, which does not allow the joint to sustain the increasingly higher peel (σ_y) and shear (τ_{xy}) peak stresses developing at both ends of the adhesive layer for higher L_O. Actually, this phenomenon is widely addressed in the literature [9] and it contrasts with the behavior of joints bonded with ductile adhesives, where a close to proportional curve can be obtained if the adhesive is sufficiently ductile. Fig. 7 also shows low standard deviations (maximum of 2.98% for L_O=50 mm), corroborating the good specimen preparation and repeatability of results.

Although the scope of the present work is restricted to the L_O analysis and ISSF validation by changing this parameter, by comparison with available experimental data, other material and geometrical variables affect P_m.

- Geometrically, apart from L_O, the main parameters to be considered are t_A and t_P. Firstly, t_A is a controversial issue in the literature regarding the associated phenomena leading to the modification of the adhesive performance with this parameter, although there is general a consensus that higher t_A reduce P_m. Some hypotheses are the higher interfacial shear stresses [48], the poorer adhesive quality due to the introduction of micro-cracks and voids [49], or even the reduction of the cohesive stresses at the crack tip [50]. On the other hand, higher t_P is often associated to improved strength, especially in joints bonded with brittle adhesives, due to more uniform stress distributions in the adhesive layer [51].
- The effect of the adhesive and adherends' material properties is also documented in the literature. Typically, and due to major stress gradients occurring in thin adhesive layers in bonded joints, strong and brittle adhesives perform well only for short L_O, for which the stress variations are smaller, while failing to compete with less strong but ductile adhesives for larger L_O. Actually, under these conditions, the peak stresses in the brittle adhesive is quickly reached at the overlap ends, and the joint fails prematurely. This issue was carefully

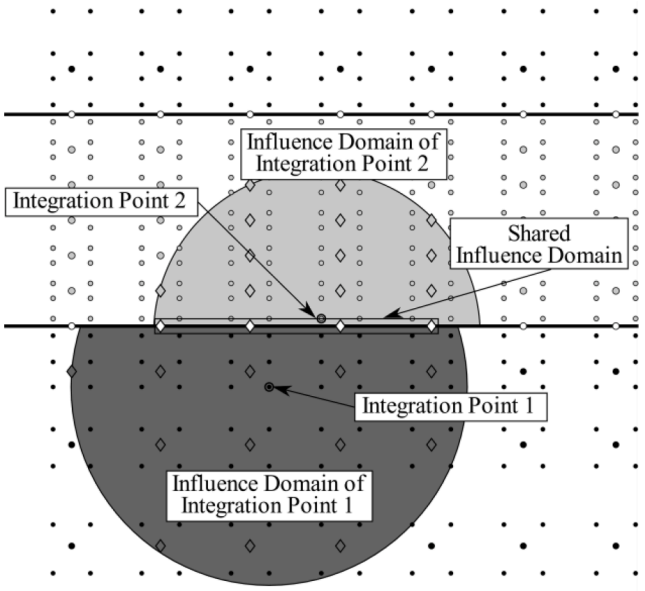

Fig. 6. Influence domains at the material interface.

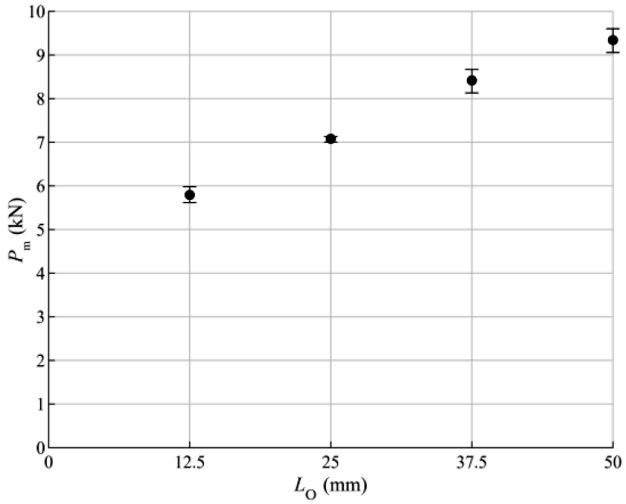

Fig. 7. P_m vs L_O plot with standard deviation.

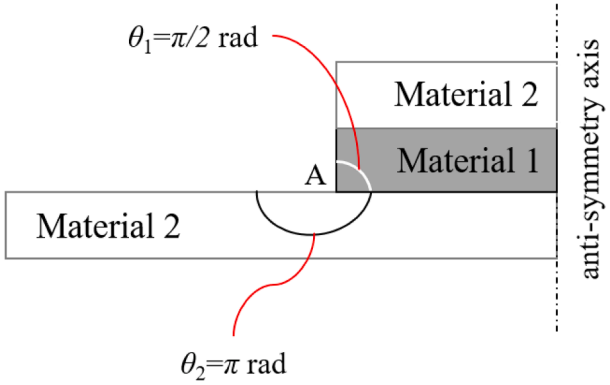

Fig. 8. SLJ corner geometry and anti-symmetry axis considered.

assessed in the work of Nunes et al. [52], showing that the brittle Araldite® AV138 can compete with a less strong but ductile adhesive (Araldite® 2015) for short L_O (12.5 mm), while not accomplishing so for larger L_O (over 25 mm). The adherend material effect is closely related to the formerly introduced t_P discussion, since higher adherend stiffness decreases peak stresses [53], and higher strength prevents adherend yielding, which can induce localized straining in the adhesive layer and lead to premature failures [54].

4.2. Determination of the stress singularities

The first step of the ISSF estimation process was to evaluate the corner geometry.

Analysing Fig. 8 and considering point A as the center of the polar coordinate system, the angle θ_1 is associated with the adhesive layer geometry. In contrast, the angle θ_2 defines the adherend geometry. Therefore $\theta_1=\pi/2$ rad and $\theta_2=\pi$ rad. This corner geometry, alongside this material combination, leads to the existence of two exponents characterising the stress singularity at the adhesive/adherend interface corner (λ_1 and λ_2). Solving Eq. (10), λ_1=0.6539 and λ_2=0.9984 are obtained. As mentioned before, in this work, an interpolation method is applied. For that, two different angles are needed to perform the extrapolation, according to Eq. (16). In this case, the following angles were chosen: $\theta_3=\pi/4$ rad and $\theta_4=-\pi/4$ rad. These angles were not randomly chosen. They are the angles that allow a nodal based H_1 and H_2 determination in the two materials. Thus, one angle is in the ascending part of the $\sigma_{\theta\theta}$ curve (θ_4) and the other one in the descending part of the same curve (θ_3).

The determination of the eigenvalues (λ_n) allowed the calculation of the parameter $f_{\theta\theta}$ for the chosen interpolation angles (θ_3 and θ_4), by Eq. (13). This parameter completes the first matrix of Eq. (16). The matrix on the right side of this equation is obtained through numerical analysis. This equation system was repeated for different radii from the interface corner. The stress singularities (H_1 and H_2) were finally calculated for the different radii considered. This calculation was performed when the reaction forces equal the experimental failure at the end where the displacement was imposed. By plotting the values from the different radii, it was perceptible that they are stable in the interval $0.01<r<0.02$ mm (close enough to the corner tip to be influenced by other corners singularities). Thus, the values of H_1 and H_2 were extrapolated by a linear function to $r=0$ mm from the values in this interval. In Fig. 9, this process was performed for the joint with L_O=37.5 mm. To determine the stress singularities for the other L_O, the extrapolations were performed at an imposed displacement where H_n (where $n=1$ or $n=2$) would be the same as the H_n of L_O=37.5 mm at failure displacement.

Fig. 9 shows the extrapolations for the different L_O with the two considered discretizations. The obtained data reveals that the results are discretization-independent since the difference in the extrapolated H_1 between the baseline and the refined mesh is around 1%. The comparison between the different L_O shows a more pronounced slope in extrapolation for larger L_O. The RPIM approach also leads to slight oscillations in the results because of the proximity to the singularity region. However, these do not affect the results since they occur outside the r interval considered to perform the extrapolations. All the presented results concern only the first singularity (H_1) since it is the most significant. Nonetheless, the determination of the second singularity component follows the same procedure. A comparison between the stress components obtained from the numerical simulations and the ones predicted by the analytical formula was also performed, as shown in Fig. 10. These were obtained at $r=0.01$ mm, and when H_1 was the same for all the L_O. From this figure, a considerable similarity is found between the numerical and analytical stresses, confirming the implemented formulation's suitability. As expected, the stress components for the different L_O are identical since the H_1 was the same for all L_O.

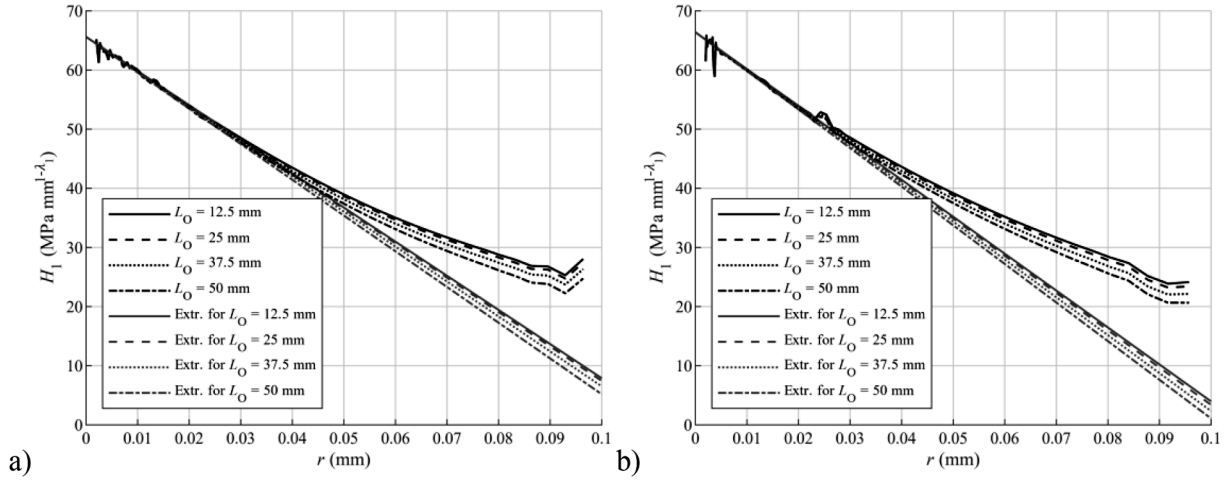

Fig. 9. Extrapolation of H_1 using the (a) baseline discretization and the (b) refined discretization.

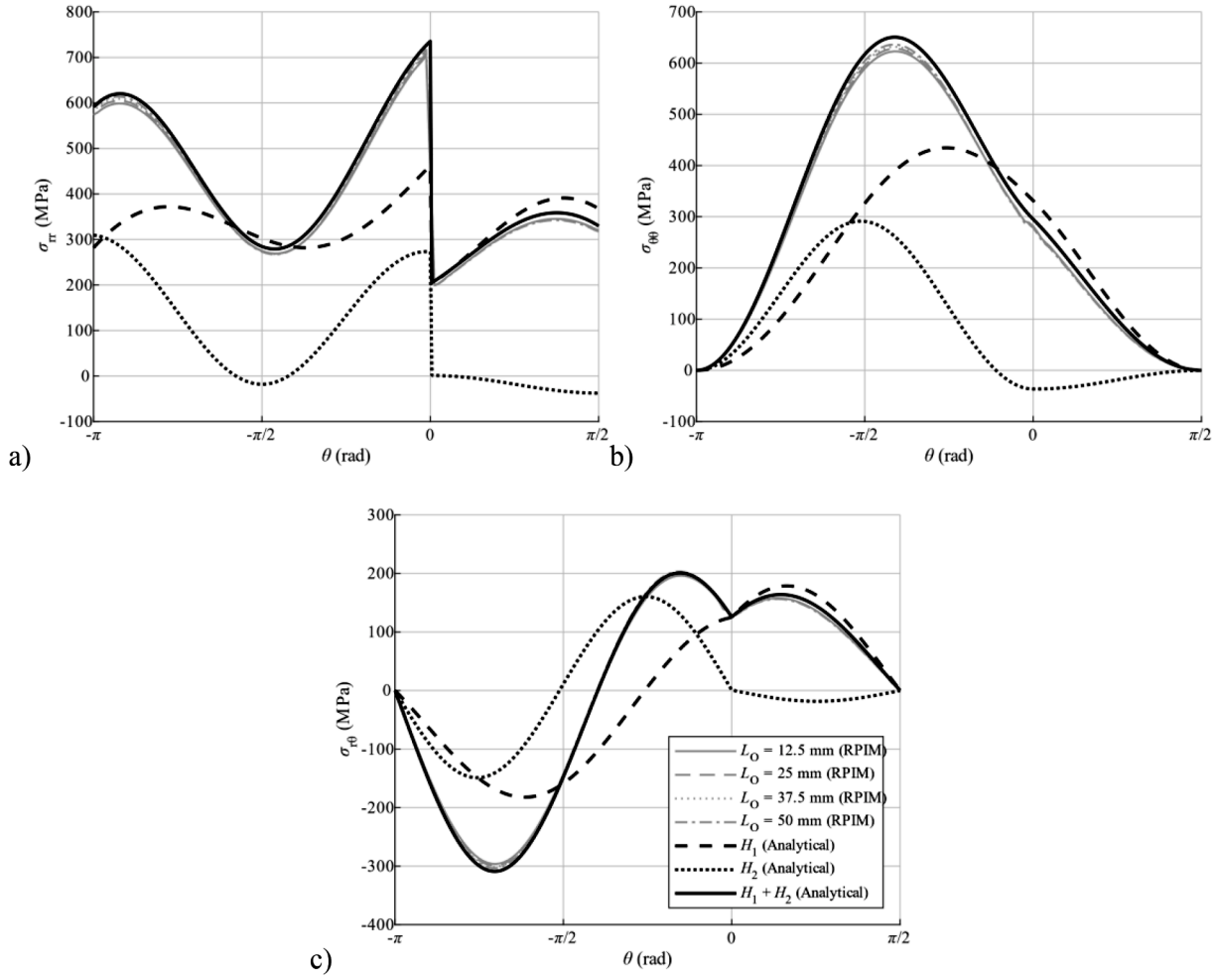

Fig. 10. Comparison between the analytical and numerical stress components: σ_{rr} (a), $\sigma_{\theta\theta}$ (b) and $\sigma_{r\theta}$ (c).

4.3. Numerical predictions

The last stage of the ISSF criterion validation was the strength prediction and comparison with the experimental results. For this purpose, it was necessary to know the critical singularity components (H_c) to compare them with the singularity components determined in the previous section. This process can be carried out through different approaches, such as the Reciprocal Work Contour Integral Method (RWCIM) [55]. However, they usually are very complicated to implement. For that reason, an inverse technique was considered, consisting of a combination between numerical simulations and experimental data. In this case, the experimentally determined failure load was used as the

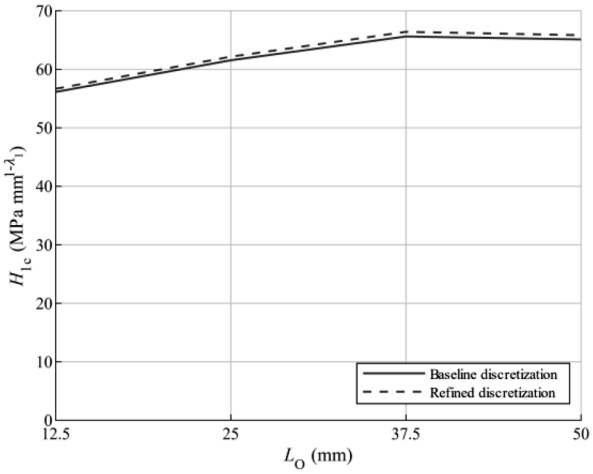

Fig. 11. H_{1c} comparison between the different L_O.

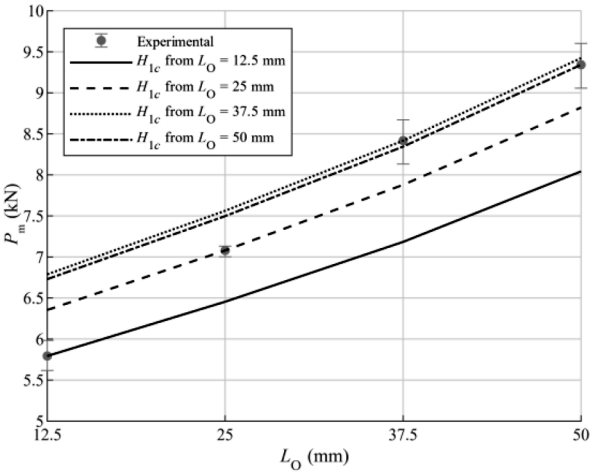

Fig. 12. Comparison between experimental and numerical P_m vs L_O.

imposed load in a numerical simulation with a given L_O. These simulations allowed the determination of the H_n values, which were then used as the H_{nc} values for the other L_O, leading to P_m estimation for all L_O. Since H_{nc} can be inferred for all L_O, this process can be repeated for the four experimentally tested L_O, giving four P_m vs L_O prediction curves.

The H_{1c} attained with this method are presented in Fig. 11 for the different L_O and the two discretizations. As previously discussed, only the H_1 singularity component is presented due to its greater relevance to the predictions' outcome. Moreover, the H_{1c} values can be considered discretization-independent since the differences between the baseline and refined meshes are at most 1%. It was also found that the H_{1c} estimates using L_O=37.5 mm and L_O=50 mm are very similar. Nonetheless, for smaller L_O, the H_{1c} results are lower, this was also observed in [26]. This behavior is because there is a small amount of plasticity in longer L_O, even in this brittle adhesive. Thus, some energy would have to be spent in plasticizing the adhesive before creating a crack. Additionally, the crack can propagate stably for a few moments in longer L_O, while for smaller L_O, the whole joint fails as soon as there is a crack.

Finally, Fig. 12 features the strength predictions where P_m was predicted using each H_{1c}. These results concern the refined mesh since they are identical to those of the baseline mesh. By analysing the P_m vs L_O plots, a slope increase is detected with each increment of L_O. This observation contradicts the experimental results, where an L_O increment leads to a slope decrease. Yet, this slope increase is minimal and does not affect the results in the L_O range tested. The strength increases with L_O for the two largest L_O are perfectly in line with the experimental results (approximately a 1 kN increase), contrary to the lower strength increases of the smaller L_O. While experimentally, a 1 kN strength increase (slightly over 1 kN) was verified, numerically, this increase was smaller than 1 kN.

Regarding the method's accuracy, it is perceptible that the strength predictions are very similar for the two largest L_O, justified by a 0.87% percentual deviation when using L_O=37.5 mm to predict the strength of the L_O=50 mm joint. The same variation was verified when L_O=50 mm was used to predict the strength of the L_O=37.5 mm joint. For these two L_O, predicting the strength with L_O=12.5 mm is the least recommended procedure, given that percentual deviations of up to 14.66% were found. Predicting the strength of the highest L_O with L_O=25 mm leads to discrepancies around 5.58%. In the L_O=12.5 mm case, the nearest prediction is when L_O=25 mm was used. However, this originates an overprediction divergence of around 9.68%. Finally, for the L_O=25 mm case, the closest prediction was found when using L_O=50 mm, with a percentual deviation of 5.91%. These differences are only verified when the strength prediction of a given L_O is attained with a different L_O since each curve is based on the experimental failure load verified for that L_O.

5. Conclusions

This work's primary purpose was the implementation and validation of the ISSF criterion by a meshless method, in this case, the RPIM, for the strength prediction of multi-material corners in adhesively bonded joints. Initially, experimental tests were performed on aluminium SLJ with different L_O, and the resulting strength data was collected to validate the proposed approach. In terms of the ISSF criterion, its implementation started with defining the interface corner's geometry, which led to two exponents characterising it (λ_1 and λ_2). Then, to determine H_n, an extrapolation method was applied, which consisted of determining these parameters for different radii and then extrapolating them to the interface corner. The results obtained in this work allow the following conclusions:

- the numerical simulations showed that this technique does not depends on the discretization density, which constitutes a significant advantage in bonded joint design. Nonetheless, the RPIM results showed some oscillations of H_1 that were not significant since they were not in the extrapolation interval;
- an inverse method was applied to determine the critical singularity components (H_{nc}) necessary for the strength prediction. This approach combined numerical simulations with experimental data and led to good results for higher L_O;
- the obtained H_{nc} values with smaller L_O showed lower strength predictions when a smaller L_O was used to predict the strength of a larger L_O. For this reason, it is advisable to only predict the strength with L_O larger than the one used to determine H_{nc}. This way, a more conservative strength prediction is attained, which is recommended due to safety reasons;
- the two highest L_O presented incredibly similar strength predictions with a percentual deviation of only 0.83%. The maximum percentual deviation was found when the H_{1c} determined with L_O=12.5 mm was used to predict the strength of the L_O=37.5 mm joint (14.66%);
- the results obtained in this work validated the use of the ISSF criterion together with meshless methods for mixed-mode bonded joint analysis;
- the proposed method for determining the H_{nc} values showed exciting results when considering its simplicity against other widespread approaches.

Declaration of Competing Interest

The authors declare no conflict of interest.

Acknowledgments

This work has been funded by the Ministério da Ciência, Tecnologia e Ensino Superior through the Fundação para a Ciência e a Tecnologia (from Portugal), under project fundings 'POCI-01–0145-FEDER-028351', and 'SFRH/BD/147628/2019'. Additionally, the authors acknowledge the funding provided by the Associated Laboratory for Energy, Transports and Aeronautics (LAETA), under project 'UIDB/50022/2020'.

Appendix 1

$$e = (\alpha-\beta)\big(\cos[2\lambda\theta_1] - \cos[2\lambda\theta_1 - 2\lambda\theta_2] + \lambda^2[\cos(2\theta_1) - \cos(2\theta_1+2\theta_2) - 1 + \cos(2\theta_2)]\big) \\ +(1+\alpha)(1-\cos[2\lambda\theta_1]) - (1-\beta)(1-\cos[2\lambda\theta_2]) \tag{17}$$

$$b = (\alpha-\beta)\big(\sin[2\lambda\theta_1] - \sin[2\lambda\theta_1 - 2\lambda\theta_2] - \lambda^2[\sin(2\theta_1) - \sin(2\theta_1+2\theta_2) + \sin(2\theta_2)]\big) \\ -(1+\alpha)\sin(2\lambda\theta_1) - (1-\beta)\sin(2\lambda\theta_2) \tag{18}$$

$$c = (\alpha-\beta)(\cos[2\lambda\theta_1] - \cos[2\lambda\theta_1 + 2\theta_2] + \cos[2\lambda\theta_2] - \cos(2\lambda\theta_2 - 2\theta_1) - 1 + \cos(2\theta_1)) \\ +(1+\alpha)(1-\cos[2\theta_1]) - (1-\beta)(1-\cos[2\theta_2]) \tag{19}$$

$$d = (\alpha-\beta)(\sin[2\theta_1] + \sin[2\lambda\theta_2 - 2\theta_1] - \sin[2\lambda\theta_1] + \sin(2\lambda\theta_1+2\theta_2) - \sin(2\theta_2)) \\ -(1+\alpha)\sin(2\theta_1) - (1-\beta)\sin(2\theta_2) \tag{20}$$

Appendix 2

$$\chi_{31} = -\cos(2\lambda\theta_1) - \lambda\cos(2\theta_1) \tag{21}$$

$$\chi_{32} = \sin(2\lambda\theta_1) - \lambda\sin(2\theta_1) \tag{22}$$

$$\chi_{41} = \sin(2\lambda\theta_1) + \lambda\sin(2\theta_1) \tag{23}$$

$$\chi_{42} = \cos(2\lambda\theta_1) - \lambda\cos(2\theta_1) \tag{24}$$

$$\chi_{51} = \frac{1-\beta+(\alpha-\beta)(\lambda-\cos(2\lambda\theta_1)-\lambda\cos(2\theta_1))}{1+\alpha} \tag{25}$$

$$\chi_{52} = \frac{(\alpha-\beta)(\sin(2\lambda\theta_1)-\lambda\sin(2\theta_1))}{1+\alpha} \tag{26}$$

$$\chi_{61} = -\frac{(\alpha-\beta)(\sin(2\lambda\theta_1)+\lambda\sin(2\theta_1))}{1+\alpha} \tag{27}$$

$$\chi_{62} = \frac{1-\beta-(\alpha-\beta)(\lambda+\cos(2\lambda\theta_1)-\lambda\cos(2\theta_1))}{1+\alpha} \tag{28}$$

$$\chi_{71} = \frac{(\alpha-\beta)(\sin[2\lambda\theta_1]+\lambda\sin[2\theta_1])(\sin[2\lambda\theta_2]-\lambda\sin[2\theta_2])}{1+\alpha} \\ -\frac{(1-\beta+[\alpha-\beta][\lambda-\cos(2\lambda\theta_1)-\lambda\cos(2\theta_1)])(\cos[2\lambda\theta_2]+\lambda\cos[2\theta_2])}{1+\alpha} \tag{29}$$

$$\chi_{72} = -\frac{(\alpha-\beta)(\sin[2\lambda\theta_1]-\lambda\sin[2\theta_1])(\cos[2\lambda\theta_2]+\lambda\cos[2\theta_2])}{1+\alpha} \\ -\frac{(1-\beta-[\alpha-\beta][\lambda+\cos(2\lambda\theta_1)-\lambda\cos(2\theta_1)])(\sin[2\lambda\theta_2]-\lambda\sin[2\theta_2])}{1+\alpha} \tag{30}$$

$$\chi_{81} = -\frac{(\alpha-\beta)(\sin[2\lambda\theta_1]+\lambda\sin[2\theta_1])(\cos[2\lambda\theta_2]-\lambda\cos[2\theta_2])}{1+\alpha} \\ -\frac{(1-\beta+[\alpha-\beta][\lambda-\cos(2\lambda\theta_1)-\lambda\cos(2\theta_1)])(\sin[2\lambda\theta_2]+\lambda\sin[2\theta_2])}{1+\alpha} \tag{31}$$

$$\chi_{82} = -\frac{(\alpha-\beta)(\sin[2\lambda\theta_1]-\lambda\sin[2\theta_1])(\sin[2\lambda\theta_2]+\lambda\sin[2\theta_2])}{1+\alpha} \\ -\frac{(1-\beta-[\alpha-\beta][\lambda+\cos(2\lambda\theta_1)-\lambda\cos(2\theta_1)])(\cos[2\lambda\theta_2]-\lambda\cos[2\theta_2])}{1+\alpha} \tag{32}$$

$$y_1 = \frac{c-e}{\lambda([\lambda+1-\cos(2\lambda\theta_1)-\lambda\cos(2\theta_1)][c-e]+b+d)} \tag{33}$$

$$y_2 = \frac{b+d}{\lambda([\lambda+1-\cos(2\lambda\theta_1)-\lambda\cos(2\theta_1)][c-e]+b+d)} \tag{34}$$

References

[1] Da Silva LF, Öchsner A, Adams RD. Handbook of adhesion technology. Berlin, Germany: Springer Science & Business Media; 2011.
[2] Ebnesajjad S, Landrock AH. Adhesives technology handbook. London, UK: William Andrew; 2014.
[3] Du J, Salmon FT, Pocius AV. Modeling of cohesive failure processes in structural adhesive bonded joints. J Adhes Sci Technol 2004;18(3):287–99.
[4] Gui C, Bai J, Zuo W. Simplified crashworthiness method of automotive frame for conceptual design. Thin Walled Struct 2018;131:324–35.
[5] Volkersen O. Die Nietkraftverteilung in zugbeanspruchten Nietverbindungen mit konstanten Laschenquerschnitten. Jahrb Dtsch Luftfahrtforsch 1938;15:41–7.
[6] da Silva LF, das Neves PJ, Adams R, Spelt J. Analytical models of adhesively bonded joints—Part I: literature survey. Int J Adhes Adhes 2009;29(3):319–30.
[7] Goland M, Reissner E. The stresses in cemented joints. J Appl Mech 1944;66: A17–27.
[8] Hart-Smith, L.J., Adhesive-bonded single-lap joints, in NASA Contract Report, NASA CR-112236. 1973. https://ntrs.nasa.gov/citations/19740005083.
[9] De Sousa CCRG, Campilho RDSG, Marques EAS, Costa M, da Silva LFM. Overview of different strength prediction techniques for single-lap bonded joints. Proc Inst Mech Eng Part L J Mater Des Appl 2017;231:210–23.
[10] Crocombe A. Global yielding as a failure criterion for bonded joints. Int J Adhes Adhes 1989;9(3):145–53.
[11] Campilho RD. Strength prediction of adhesively-bonded joints. Boca Raton, U.S.: CRC Press; 2017.
[12] Razavi SMJ, Ayatollahi MR, Majidi HR, Berto F. A strain-based criterion for failure load prediction of steel/CFRP double strap joints. Compos Struct 2018;206: 116–23.
[13] Kim MH, Hong HS. An adaptation of mixed-mode I+ II continuum damage model for prediction of fracture characteristics in adhesively bonded joint. Int J Adhes Adhes 2018;80:87–103.
[14] Santos T, Campilho R. Numerical modelling of adhesively-bonded double-lap joints by the extended finite element method. Finite Elem Anal Des 2017;133:1–9.
[15] Ramalho LDC, Campilho RDSG, Belinha J, da Silva LFM. Static strength prediction of adhesive joints: a review. Int J Adhes Adhes 2020;96:102451.
[16] Da Silva LFM, Campilho RDSG. Advances in numerical modelling of adhesive joints. Advances in numerical modeling of adhesive joints. Heidelberg: Springer; 2012.
[17] Zhang J, Wang J, Yuan Z, Jia H. Effect of the cohesive law shape on the modelling of adhesive joints bonded with brittle and ductile adhesives. Int J Adhes Adhes 2018;85:37–43.
[18] Rice JR. A path independent integral and the approximate analysis of strain concentration by notches and cracks. J Appl Mech 1968;35(2):379–86.
[19] Rybicki EF, Kanninen MF. A finite element calculation of stress intensity factors by a modified crack closure integral. Eng Fract Mech 1977;9(4):931–8.
[20] Leguillon D. Strength or toughness? A criterion for crack onset at a notch. Eur J Mech A Solids 2002;21(1):61–72.
[21] Williams ML. The stresses around a fault or crack in dissimilar media. Bull Seismol Soc Am 1959;49(2):199–204.
[22] Bogy DB. Edge-bonded dissimilar orthogonal elastic wedges under normal and shear loading. J Appl Mech 1968;35(3):460–6.
[23] Noda N, Li R, Miyazaki T, Takaki R, Sano Y. Convenient adhesive strength evaluation method in terms of the intensity of singular stress field. Int J Comput Methods 2019;16(01):1850085.
[24] Goglio L, Rossetto M. Stress intensity factor in bonded joints: influence of the geometry. Int J Adhes Adhes 2010;30(5):313–21.
[25] Askarinejad S, Thouless MD, Fleck NA. Failure of a pre-cracked epoxy sandwich layer in shear. Eur J Mech A Solids 2021;85:104134.
[26] Akhavan-Safar A, Ayatollahi MR, Rastegar S, da Silva LFM. Impact of geometry on the critical values of the stress intensity factor of adhesively bonded joints. J Adhes Sci Technol 2017;31(18):2071–87.
[27] Liu GR, Gu YT. An introduction to meshfree methods and their programming. Dordrecht, The Netherlands: Springer Science & Business Media; 2005.
[28] Wang J, Liu G. A point interpolation meshless method based on radial basis functions. Int J Numer Methods Eng 2002;54(11):1623–48.
[29] Dinis L, Jorge RN, Belinha J. Analysis of 3D solids using the natural neighbour radial point interpolation method. Comput Methods Appl Mech Eng 2007;196 (13–16):2009–28.
[30] Belinha J. Meshless methods in biomechanics: bone tissue remodelling analysis, 16. Switzerland: Springer; 2014.
[31] Farahani BV, Tavares PJ, Moreira PMGP, Belinha J. Stress intensity factor calculation through thermoelastic stress analysis, finite element and RPIM meshless method. Eng Fract Mech 2017;183:66–78.
[32] Ramalho L, Sánchez-Arce I, Campilho R, Belinha J, Silva F. Strength prediction and stress analysis of adhesively bonded composite joints using meshless methods. Procedia Manuf 2020;51:904–11.
[33] Sánchez-Arce I, Ramalho L, Campilho R, Belinha J. Analyzing single-lap joints bonded with a brittle adhesive by an elastic meshless method. Procedia Struct Integr 2020;28:1084–93.
[34] Wen PH, Tang YD, Sladek J, Sladek V. BEM analysis for curved cracks. Eng Anal Bound Elem 2021;127:91–101.
[35] Useche J, Medina C. Boundary element analysis of laminated composite shear deformable shallow shells. Compos Struct 2018;199:24–37.
[36] Shiah YC, Hematiyan MR. Interlaminar stresses analysis of three-dimensional composite laminates by the boundary element method. J Mech 2018;34(6): 829–37.
[37] Jia PH, Lei L, Hu J, Chen Y, Han K, Huang WF, Nie Z, Liu QH. Twofold domain decomposition method for the analysis of multiscale composite structures. IEEE Trans Antennas Propag 2019;67(9):6090–103.
[38] Campilho RDSG, Banea MD, Pinto AMG, da Silva LFM, De Jesus AMP. Strength prediction of single-and double-lap joints by standard and extended finite element modelling. Int J Adhes Adhes 2011;31(5):363–72.
[39] Campilho RDSG, Pinto AMG, Banea MD, Silva RF, da Silva LFM. Strength improvement of adhesively-bonded joints using a reverse-bent geometry. J Adhes Sci Technol 2011;25(18):2351–68.
[40] Bathe KJ. Finite element procedures. Klaus-Jurgen Bathe; 2006.
[41] Liu GR. A point assembly method for stress analysis for two-dimensional solids. Int J Solids Struct 2002;39(1):261–76.
[42] Wang JG, Liu GR. On the optimal shape parameters of radial basis functions used for 2-D meshless methods. Comput Methods Appl Mech Eng 2002;191(23–24): 2611–30.
[43] Qian Z, Akisanya A. Wedge corner stress behaviour of bonded dissimilar materials. Theor Appl Fract Mech 1999;32(3):209–22.
[44] Dundurs J. Edge-bonded dissimilar orthogonal elastic wedges under normal and shear loading. J Appl Mech 1969;35:460–6.
[45] Liu GR. Meshfree methods. Boca Raton: CRC Press; 2010.
[46] Cordes LW, Moran B. Treatment of material discontinuity in the element-free Galerkin method. Comput Methods Appl Mech Eng 1996;139(1–4):75–89.
[47] Ramalho LDC, Campilho RDSG, Belinha J. Single lap joint strength prediction using the radial point interpolation method and the critical longitudinal strain criterion. Eng Anal Bound Elem 2020;113(January):268–76.
[48] Gleich DM, Van Tooren MJL, Beukers A. Analysis and evaluation of bondline thickness effects on failure load in adhesively bonded structures. J Adhes Sci Technol 2001;15(9):1091–101.
[49] Adams R, Peppiatt N. Stress analysis of adhesive-bonded lap joints. J Strain Anal 1974;9(3):185–96.
[50] Ji G, Ouyang Z, Li G, Ibekwe S, Pang SS. Effects of adhesive thickness on global and local Mode-I interfacial fracture of bonded joints. Int J Solids Struct 2010;47 (18–19):2445–58.
[51] Campilho RDSG, De Moura MFSF, Domingues JJMS. Modeling single and double-lap repairs on composite materials. Compos Sci Technol 2005;65(13):1948–58.
[52] Nunes SLS, Campilho RDSG, Da Silva FJG, De Sousa CCRG, Fernandes TAB, Banea MD, Da Silva LFM. Comparative failure assessment of single and double lap joints with varying adhesive systems. J Adhes 2016;92(7–9):610–34.
[53] Aydin MD, Özel A, Temiz Ş. The effect of adherend thickness on the failure of adhesively-bonded single-lap joints. J Adhes Sci Technol 2005;19(8):705–18.
[54] Fernandes TAB, Campilho RDSG, Banea MD, da Silva LFM. Adhesive selection for single lap bonded joints: experimentation and advanced techniques for strength prediction. J Adhes 2015;91(10–11):841–62.
[55] Galvez P, Noda NA, Takaki R, Sano Y, Miyazaki T, Abenojar J, Martínez MA. Intensity of singular stress field (ISSF) variation as a function of the Young's modulus in single lap adhesive joints. Int J Adhes Adhes 2019;95:102418.